Saturation of the Two-Plasmon Decay Instability in Long-Scale-Length Plasmas Relevant to Direct-Drive Inertial Confinement Fusion

D. H. Froula,* B. Yaakobi, S. X. Hu, P-Y. Chang, R. S. Craxton, D. H. Edgell, R. Follett, D. T. Michel, J. F. Myatt, W. Seka, R. W. Short, A. Solodov, and C. Stoeckl

Laboratory for Laser Energetics, University of Rochester, Rochester, New York 14636, USA

(Received 19 September 2011; published 18 April 2012)

Measurements of the hot-electron generation by the two-plasmon-decay instability are made in plasmas relevant to direct-drive inertial confinement fusion. Density-scale lengths of 400 μm at $n_{cr}/4$ in planar CH targets allowed the two-plasmon-decay instability to be driven to saturation for vacuum intensities above $\sim 3.5 \times 10^{14}$ W cm^{-2}. In the saturated regime, $\sim 1\%$ of the laser energy is converted to hot electrons. The hot-electron temperature is measured to increase rapidly from 25 to 90 keV as the laser beam intensity is increased from 2 to 7×10^{14} W cm^{-2}. This increase in the hot-electron temperature is compared with predictions from nonlinear Zakharov models.

DOI: 10.1103/PhysRevLett.108.165003 PACS numbers: 52.38.Kd, 41.75.Jv, 52.35.Mw

Direct-drive inertial confinement fusion is an encouraging path to high-gain inertial fusion energy [1]. In the direct-drive approach to inertial confinement fusion, high-power, moderate intensity laser beams ($\sim 7 \times 10^{14}$ W cm^{-2}) produce and propagate through a high-temperature ($T_e \sim 3.5$ keV) long-scale-length ($L_n \sim 500$ μm) underdense plasma prior to depositing energy near the critical surface of a spherical capsule. A series of shocks are launched which adiabatically compress the nuclear fuel to fusion conditions [2–4]. For the most efficient compression, the shocks are driven on a low adiabat [5], and ignition is susceptible to preheat; heating of the unablated fuel by ''hot'' electrons increases the implosion adiabat, reducing the compression efficiency. Typical direct-direct-drive ignition designs can withstand on the order of 0.1% of the laser energy converted to preheat [6].

Electrons can be accelerated to high energies by the two-plasmon decay (TPD) instability [7] in which the incident electromagnetic wave decays into two electron plasma waves [8–10]. The instability grows rapidly through the resonant coupling of the electric field of the incident laser beam and the longitudinal electrostatic field of the two electron plasma waves. The dependence of the TPD growth on the hydrodynamic conditions is evident in the convective (intensity) gain exponent for the instability of a single plane electromagnetic wave parallel to the density gradient [$G_{SB} \simeq 2.1 \times 10^{-2} I_s(\times 10^{14}$ W cm$^{-2}) L_n(\mu\text{m})/T_e(\text{keV})$, where I_s is the single laser beam intensity, L_n is the density-scale length, T_e is the electron temperature, and all parameters are taken at $n_{cr}/4$, $n_{cr} \simeq 10^{22}$ cm^{-3}] [11–13]. Simulations based on a nonlinear Zakharov model [14] indicate that electrons are stochastically accelerated to high energies (> 50 keV) by enhanced electron plasma waves. Once above threshold, the hot-electron temperature is shown to scale with $I_q L_n/T_e$ [15], where I_q is the overlapped laser intensity at quarter critical.

Early experiments using CO_2 lasers measured the first hot electrons generated by TPD [16] and the associated electron plasma waves by using Thomson scattering [17]. More recent experiments focusing on TPD in direct-drive ignition conditions [18] demonstrated that the efficiency of hot-electron generation scaled with overlapped-laser-beam intensity [19]. Furthermore, these studies showed a nearly constant hot-electron temperature [20] and saturation of the hot-electron generation at 0.1% of the incident laser energy when plotted against the vacuum laser intensity. This apparent saturation and low level of electron generation were a result of the hydrodynamics; the small laser spots used to produce the highest intensities limited the scale length to less than $L_n < 200$ μm. When taking this into account, the ratio of the drive intensity to the threshold did not change appreciably (i.e., $I_q L_n/T_e \sim$ const). In general, the maximum scale length at quarter critical is given by half of the diameter of the laser beams spot, and Fig. 1(a) shows that increasing the diameter of the laser beams while maintaining a constant intensity allows $I_q L_n/T_e$ be increased.

In this Letter, we present the first measurements of a rapid increase in the hot-electron temperature (25–90 keV) while driving the two-plasmon decay instability to saturation at direct-drive ignition plasma conditions. The large laser spots and high intensities used in these experiments produced a 400 μm long-scale-length 2.5 keV plasma where $I_q L_n/T_e$ is increased by nearly a factor of 4 when the laser intensity is varied from 1.3 to 7×10^{14} W cm^{-2}. These long-scale lengths led to a low intensity ($< 1.3 \times 10^{14}$ W cm^{-2}) onset of hot-electron generation which is driven to saturation ($\sim 1\%$) for intensities above 3×10^{14} W cm^{-2}. Thomson scattering is used to validate the hydrodynamic modeling by measuring the electron temperature at quarter critical. The rapid increase in hot-electron temperature is compared with simulations that use

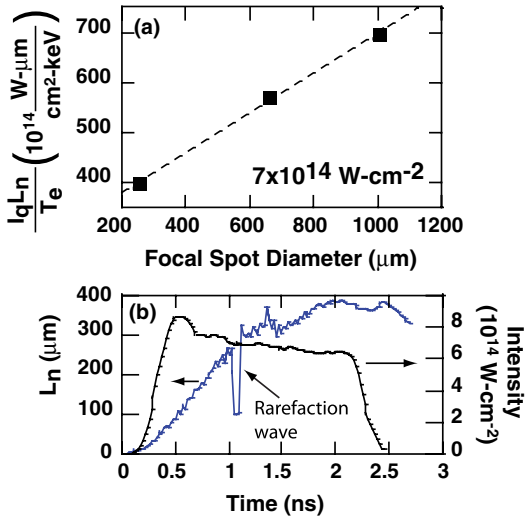

FIG. 1 (color online). (a) The calculated plasma parameters as a function of the diameter of the laser beams, at constant intensity (7×10^{14} W cm^{-2}), demonstrates that the high intensities over large laser spots available in these experiments allow the TPD parameter ($I_q L_n/T_e$) to be extended to direct-drive ignition conditions. (b) At the conditions for this experiment (1000 μm diameter laser spot), the density-scale length (left axis) is calculated to reach nearly 400 μm for the highest intensities tested (right axis).

a Zakharov model designed to provide a physics-based predictive capability for TPD at ignition conditions.

For this study, four ultraviolet (3ω, $\lambda = 0.35$ μm) beams available from the OMEGA EP [21] produced the required intensities over a large-diameter laser spot ($\sim$ 1 mm), to create 400 μm plasma density-scale lengths at $n_{cr}/4$ [Fig. 1(b)]. The long-scale-length CH plasma is produced by illuminating a 30-μm-thick CH layer deposited on 30 μm of Mo and backed with an additional 30 μm of CH target.

Two-dimensional hydrodynamic simulations using the code DRACO [22] show that the maximum achievable scale length in planar geometry is obtained by maximizing the overlapped-laser-beam intensity while providing enough time for the plasma to reach the steady state [Fig. 1(b)]. For the highest laser beam energies available at 2 ns, the optimal laser spot size is $\sim$1 mm in diameter—a further increase in laser spot size reduces the intensity on target resulting in a shorter scale length. For the experimental conditions presented here, the scale length reaches a steady state after about 1.5 ns, and the asymptotic scale length is given by $L_n \simeq 250$ μm$(I_{14})^{1/4}$.

A maximum overlapped laser intensity of 7×10^{14} W cm^{-2} was achieved by using a total energy on target of 8.7 kJ in a 2-ns flattop laser pulse [Fig. 1(b)]. The four UV beams are incident on the target at an angle of 23° with respect to the target normal and are linearly polarized in the same direction. Two sets of distributed phase plates [23] were used (840 and 890 μm diameter measured at the $1/e$ intensity points) to produce a combined intensity distribution that has a super-Gaussian profile with a diameter of nearly 1 mm.

Figure 2 shows a Thomson scattering spectrum that provides a measure of the electron and ion temperature as a function of time at the 3ω quarter critical surface. The rarefaction wave launched from the CH-Mo interface is observed in the Thomson scattering spectrum 1.11 ns after the laser beams turns on, which is in excellent agreement with the hydrodynamic simulations [Fig. 1(b)]. Although the density-scale length at quarter critical is not directly measured, the excellent agreement between the measured and simulated time of arrival of the rarefaction wave demonstrates the accuracy of the thermal conduction model and is a strong indication that the calculated density and temperature profiles are accurate.

The Thomson scattering measurements were obtained on the OMEGA laser system by using the same target platform and pulse shape and similar laser beam diameters (800 μm FWHM) as used on the OMEGA EP experiments. A 20 J, $\lambda_{4\omega} = 0.26$ μm, $f/6.7$ Thomson scattering probe beam was focused to a diameter of 60 μm, and the Thomson scattered light was collected from a $60 \times 75 \times 75$ μm^3 volume located 200 μm from the initial target surface [24]. The Thomson scattering diagnostic probes ion-acoustic waves propagating nearly parallel (within $\sim$10°) to the target surface [$k_a = 2k_{4\omega} \sin(\theta/2)$, where $k_{4\omega} = 2\pi/\lambda_{4\omega}$ and $\theta = 63°$ is the scattering angle].

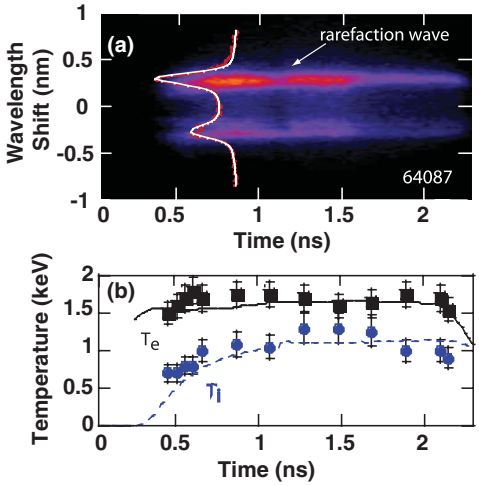

FIG. 2 (color). (a) Thomson scattered light from near the quarter critical density for 3ω light is spectrally and temporally resolved to measure the ion-acoustic features. The electron and ion temperatures as a function of time are obtained by fitting the standard dynamic form factor [31] to the measured spectra that are averaged over 50 ps. A best fit (white curve) to the measured spectrum at 0.8 ns (red curve) is obtained for $T_e = 1.6$ keV, $T_i = 1.0$ keV. (b) The electron (solid line) and ion (dashed line) temperatures calculated by DRACO compare well to the measurements. The data are obtained for an intensity of 3×10^{14} W cm^{-2}.

The energy in the Mo $K\alpha$ emission line ($E_{K\alpha}$) was measured by using an absolutely calibrated planar LiF crystal spectrometer that views the target from the incident laser side at an angle of 63° from the target normal [25]. The hot-electron temperature ($T_{\rm hot}$) is determined from the slope of the hard x-ray radiation that is assumed to be exponentially decreasing [$\exp(-E/T_{\rm hot})$]. Monte Carlo simulations show that the hard x-ray spectrum, in this energy range, provides a good estimate to the incident electron spectrum [25]. The time-integrated x-ray radiation above ~40, ~60, and ~80 keV are obtained by using a three-channel scintillator detector (HXRD). The ratio of the signals obtained for each pair of channels provides a measure of the hot-electron temperature, and a χ^2 analysis using the three measured signals is performed to determine the best hot-electron temperature [26]. For example, the ratios between S_{60}/S_{40}, S_{80}/S_{40}, and S_{80}/S_{60} result in hot-electron temperatures of 76, 78, and 82 keV, respectively, for the data taken at an intensity of 6.8×10^{14} W cm^{-2}. The χ^2 analysis determines 77 keV. The fact that the three ratios are virtually the same testifies that the spectrum is indeed exponential. The error in the measurement of the hot-electron temperature is 20% and is dominated by the uncertainties in the relative sensitivities of the three channels.

Figure 3 shows the time history of the x-ray radiation above 40 keV measured by the HXRD. At the highest overlapped-laser-beam intensity (7×10^{14} W cm^{-2}), the hard x-ray signal increases rapidly ~0.5 ns after the laser turns on. For an intensity of 2.4×10^{14} W cm^{-2}, the signal is a factor of ~200 smaller.

Monte Carlo simulations using the code EGSnrc [27] are used to relate the measured Mo $K\alpha$ energy to the total energy in fast electrons. The 17-keV Mo $K\alpha$ line is sufficiently high in energy to ensure that photoexcitation from the $T_e \simeq 2.5$ keV coronal plasma region does not contribute to the $K\alpha$ emission measurements. This ensures that the measured $K\alpha$ emission is a result of K-shell impact and hard x-ray photoionization caused by the hot electrons produced by TPD. For the electron spectra discussed in this Letter ($T_{\rm hot} = 20$–100 keV), the Monte Carlo simulations indicate that, for a given hot-electron temperature and specific experimental geometry, the total electron energy is directly related to the total $K\alpha$ energy: $E_{\rm electrons}(\mathrm{J}) \approx 150 E_{K\alpha}(\mathrm{mJ/sr})/\sqrt{T_{\rm hot}(\mathrm{keV})}$. Furthermore, the simulations show that electrons with energies less than 120 keV are stopped within the Mo, resulting in nearly all of the electrons accelerated by TPD being absorbed in the target.

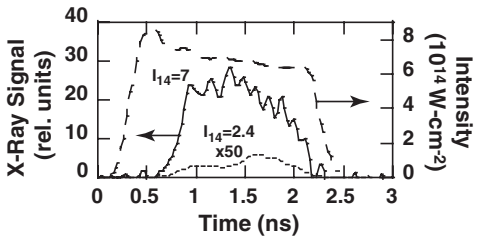

FIG. 3. The measured time history of the hard x-ray emission (> 40 keV) is shown for (solid line) 7×10^{14} (right axis) and (dots) 2.4×10^{14} W cm^{-2}.

Figure 4(a) shows that the fraction of laser energy converted into hot electrons scales exponentially with $I_q L_n/T_e$ over nearly 3 orders of magnitude when the vacuum overlapped laser intensity is varied from 1.3 to 3×10^{14} W cm^{-2} and continues to grow at a slower rate as the vacuum intensity is extended to 7×10^{14} W cm^{-2}. Over this entire range, the hydrodynamic simulations indicate that the overlapped intensity of the laser beams at $n_{\rm cr}/4$, where TPD has the largest growth rate, is reduced from the vacuum intensity by ~55% ,while the density-scale length and the electron temperature at the same location increased from 1.4 to 2.5 keV and 280 to 400 μm, respectively. The large fraction of laser energy converted into hot electrons and its observed saturation are a direct consequence of the simultaneous high intensity and long-scale lengths produced in these experiments.

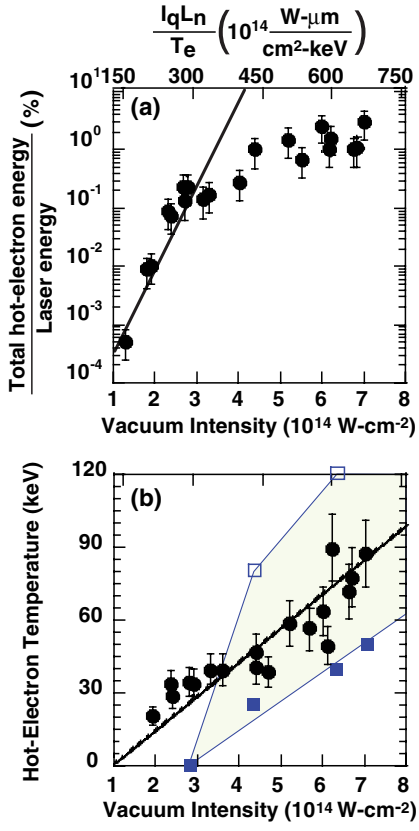

FIG. 4 (color online). (a) The fraction of total laser energy deposited into the hot electrons is plotted as a function of the vacuum intensity (bottom axis) and $I_q L_n/T_e$ (top axis). (b) The hot-electron temperature inferred from the HXRD hard x-ray measurements (circles) is shown. The hot-electron temperatures calculated by ZAK (open squares) and QZAK (solid squares) are included for reference.

Figure 4(b) shows that the hot-electron temperature increases from 25 to 90 keV as the laser intensity is increased from 2 to 7×10^{14} W cm^{-2}. These experimental results are compared with calculations from two theoretical models of two-plasmon decay instability for the exact parameters of the experiment. The open squares are results obtained from the code ZAK [13], which solves the equations of the extended Zakharov model [14]. The saturating nonlinearities included in the model are density profile modification [28], Langmuir wave cavitation [29], and the generation of ion-acoustic turbulence [13,15]. While this plasma-fluid model is able to describe the growth and nonlinear saturation of the instability, it does not include kinetic effects responsible for hot-electron generation. An estimate for the hot-electron temperature is instead obtained from the nonlinearly saturated state via the integration of test-electron trajectories in the electrostatic fields associated with the Langmuir turbulence (see Ref. [15] for more details).

The electron plasma wave spectrum at saturation is found to be very broad, extending from small wave numbers up to the Landau cutoff ($k\lambda_D = 0.25$). When the effect of the turbulent electron plasma wave spectrum on hot-electron production is investigated by integrating electron test particle trajectories [15], the heating is found to be diffusive for electrons above a threshold energy corresponding to the smallest phase velocity plasma waves (those at the Landau cutoff, $1/2m_e v_\phi^2 \sim 20$–30 keV). The rate of diffusion (heating) was found to scale with $I_q L_n/T_e$ as a result of the interplay between the rms plasma wave amplitudes and the available acceleration length [15].

The solid squares show the results of a generalization of the ZAK model, called QZAK, currently under development, where kinetic effects are taken into account self-consistently in the quasilinear approximation [30]. The addition of kinetic effects reduces the amplitude of the electron plasma waves reducing the hot-electron temperature for a given $I_q L_n/T_e$. The difference between the two model predictions highlights the difficulty in making predictive calculations of a highly turbulent and complex physical system.

The target platform used in these experiments was designed to account for all of the hot electrons generated by TPD, and, in general, the coupling of hot electrons to a fusion target (preheat) will be reduced by the electron divergence, a geometric factor depending on the distance between where the electrons are created and where they are absorbed, the energy distribution of the electrons, and other loss mechanisms. The planar nature of these experiments, the fact that the laser beams are at near normal incidence to the target, and that they are linearly polarized in a common direction without polarization smoothing all tend to maximize the hot-electron generation.

In summary, the high laser intensities generated over 1-mm diameter laser spots produced 400 μm long density-scale length plasmas that allowed two-plasmon decay to be driven to saturation. The hot-electron temperature is measured to increase rapidly (25–90 keV) with increasing laser beam intensity [(2–7) $\times 10^{14}$ W cm^{-2}]. The total energy in fast electrons generated by TPD is measured to increase exponentially and saturates at a level of $\sim$1% of the laser energy. The comparison of these experimental results, in the ignition relevant regime, with current TPD simulation tools constrains the theoretical or numerical models of hot-electron generation by TPD. This is of paramount importance, because these models are being used to explore strategies for the mitigation of hot-electron production in direct-drive inertial confinement fusion.

We acknowledge the OMEGA EP operations team whose efforts provided the increased laser power necessary for these results. This work was supported by the U.S. Department of Energy Office of Inertial Confinement Fusion under Cooperative Agreement No. DE-FC52-08NA28302, the University of Rochester, and the New York State Energy Research and Development Authority.

*dfroula@lle.rochester.edu

[1] J. Nuckolls, L. Wood, A. Thiessen, and G. Zimmerman, Nature (London) **239**, 139 (1972).
[2] R. L. McCrory *et al.*, Phys. Plasmas **15**, 055503 (2008).
[3] T. R. Boehly, V. N. Goncharov, W. Seka, M. A. Barrios, P. M. Celliers, D. G. Hicks, G. W. Collins, S. X. Hu, J. A. Marozas, and D. D. Meyerhofer, Phys. Rev. Lett. **106**, 195005 (2011).
[4] J. D. Lindl, P. A. Amendt, R. L. Berger, S. G. Glendinning, S. H. Glenzer, S. W. Haan, R. L. Kauffman, O. L. Landen, and L. J. Suter, Phys. Plasmas **11**, 339 (2004).
[5] V. N. Goncharov *et al.*, Phys. Rev. Lett. **104**, 165001 (2010).
[6] J. H. Kelly *et al.*, J. Phys. IV (France) **133**, 75 (2006).
[7] H. Figueroa, C. Joshi, H. Azechi, N. A. Ebrahim, and K. Estabrook, Phys. Fluids **27**, 1887 (1984).
[8] M. V. Goldman, Ann. Phys. (Leipzig) **38**, 117 (1966).
[9] C. S. Liu, M. N. Rosenbluth, and R. B White, Phys. Rev. Lett. **31**, 697 (1973).
[10] B. B. Afeyan and E. A. Williams, Phys. Plasmas **4**, 3827 (1997).
[11] M. N. Rosenbluhth, R. B. White, and C. S. Liu, Phys. Rev. Lett. **31**, 1190 (1973).
[12] A. Simon, R. W. Short, E. A. Williams, and T. Dewandre, Phys. Fluids **26**, 3107 (1983).
[13] R. Yan, A. V. Maximov, C. Ren, and F. S. Tsung, Phys. Rev. Lett. **103**, 175002 (2009).
[14] D. A. Russell and D. F. DuBois, Phys. Rev. Lett. **86**, 428 (2001); D. F. DuBois, D. A. Russell, and H. A. Rose, Phys. Rev. Lett. **74**, 3983 (1995).
[15] J. F. Myatt, J. Zhang, J. A. Delettrez, A. V. Maximov, R. W. Short, W. Seka, D. H. Edgell, D. F. DuBois, D. A. Russell, and H. X. Vu, Phys. Plasmas **19**, 022707 (2012).
[16] N. A. Ebrahim, H. A. Baldis, C. Joshi, and R. Benesch, Phys. Rev. Lett. **45**, 1179 (1980).

[17] H. A. Baldis and C. J. Walsh, Phys. Rev. Lett. **47**, 1658 (1981).
[18] W. Seka, D. H. Edgell, J. F. Myatt, A. V. Maximov, V. N. Goncharov, and H. A. Baldis, Phys. Plasmas **16**, 052701 (2009).
[19] C. Stoeckl, R. E. Bahr, B. Yaakobi, W. Seka, S. P. Regan, R. S. Craxton, J. A. Delettrez, R. W. Short, J. Myatt, A. V. Maximov, and H. Baldis, Phys. Rev. Lett. **90**, 235002 (2003).
[20] An analytical error in the analysis of the HXRD used in Ref. [19] was identified, and when corrected the hot-electron temperatures are reduced by ~40%.
[21] M. J. Guardalben *et al.*, Laboratory for Laser Energetics, 2010 (unpublished).
[22] P. B. Radha, V. N. Goncharov, T. J. B. Collins, J. A. Delettrez, Y. Elbaz, V. Y. Glebov, R. L. Keck, D. E. Keller, J. P. Knauer, and J. A. Marozas, Phys. Plasmas **12**, 056307 (2005).
[23] T. J. Kessler, Y. Lin, J. J. Armstrong, and B. Velazquez, in *Laser Coherence Control: Technology and Applications*, edited by H. T. Powell and T. J. Kessler (SPIE, Bellingham, WA, 1993), Vol. 1870, pp. 95–104.
[24] D. H. Froula, J. S. Ross, L. Divoland, and S. H Glenzer, Rev. Sci. Instrum. **77**, 10E522 (2006).
[25] B. Yaakobi, P.-Y. Chang, S. Hu, R. S. Craxton, J. Myatt, D. H. Edgell, C. Stoeckl, and D. H. Froula, Phys. Plasmas **19**, 012704 (2012).
[26] C. Stoeckl, V. Y. Glebov, D. D. Meyerhofer, W. Seka, B. Yaakobi, R. P. J. Town, and J. D. Zuegel, Rev. Sci. Instrum. **72**, 1197 (2001).
[27] I. Kawrakow, and D. W. O. Rogers, NRC Report No. PIRS-701, 2003.
[28] A. B. Langdon, B. Lasinski, and W. L. Kruer, Phys. Rev. Lett. **43**, 133 (1979).
[29] G. D. Doolen, D. F. DuBois, and H. A. Rose, Phys. Rev. Lett. **54**, 804 (1985).
[30] K. Y. Sanbonmatsu, H. X. Vu, D. F. DuBois, and B. Bezzerides, Phys. Rev. Lett. **82**, 932 (1999).
[31] D. H. Froula, G. H. Glenzer, N. C. Luhmann, and J. Sheffield, *Plasma Scattering of Electromagnetic Radiation: Theory and Measurement Techniques* (Elsevier, Burlington, MA, 2011).